Applied Surface Science 569 (2021) 151082

Contents lists available at ScienceDirect

Applied Surface Science

journal homepage: www.elsevier.com/locate/apsusc

Full Length Article

Novel two-step synthesis method of thin film heterojunction of BiOBr/Bi_2WO_6 with improved visible-light-driven photocatalytic activity

Anna Pancielejko [a,*], Justyna Łuczak [a], Wojciech Lisowski [c], Adriana Zaleska-Medynska [b], Paweł Mazierski [b,*]

[a] Department of Process Engineering and Chemical Technology, Faculty of Chemistry, Gdańsk University of Technology, G. Narutowicza 11/12, Gdansk 80-233, Poland
[b] Department of Environmental Technology, Faculty of Chemistry, University of Gdańsk, Wita Stwosza 63, Gdansk 80-233, Poland
[c] Institute of Physical Chemistry, Polish Academy of Science, Kasprzaka 44/52, Warsaw 01-244, Poland

ARTICLE INFO

Keywords:
$BiOBr/Bi_2WO_6$
Thin film
p-n heterojunction
Ionic liquid
Phenol degradation

ABSTRACT

A novel two-step ionic liquid assisted procedure was applied for a controllable synthesis of $BiOBr/Bi_2WO_6$ heterojunction thin films. The preparation route involved an anodic oxidation of tungsten foil and hydrothermal transformation of as-anodized oxide in the presence of bismuth precursor and ionic liquid, N-butylpyridinium bromide [BPy][Br]. The BiOBr plates with irregular shapes adhered to the surface of flower-like Bi_2WO_6 and formed a heterojunction between BiOBr and Bi_2WO_6, as confirmed by the analysis of their structure and composition. The highest efficiency of phenol degradation was achieved when the highest amount of IL was used (the apparent quantum efficiency was almost 8 and 71.5 times higher compared to BiOBr and Bi_2WO_6, respectively). In addition, superoxide radicals ($^{\bullet}O_2^-$) were found as the main factor responsible for the photodegradation. A possible reaction mechanism was further investigated as a function of monochromatic irradiation to determine the exact range of the composite photoactivity.

1. Introduction

Recently, bismuth-based photocatalytic materials have attracted a lot of attention in favour of their use due to their superior properties, such as controllable morphology, visible light photoresponse, and higher photoquantum yields compared with the first and most investigated photocatalyst, titanium dioxide[1,2]. Compared with metal oxide's electronic structure whose valance band (VB) usually consists of O2p orbitals, the VB of bismuth-based semiconductors is composed of O2p and Bi6s hybrid orbitals. The presence of Bi6s orbitals is beneficial for enhanced photocatalytic performance since it has influence on (i) the increased mobility of the photogenerated electron-hole pairs, and (ii) the decreased of energy band gap[1]. Among the various analysed systems, bismuth tungstate (Bi_2WO_6), one of the simplest Aurivillius oxides, an n-type semiconductor, has shown an improved efficiency in photocatalytic water splitting reaction and organic pollutants degradation in the visible range [3]. Up to now, a number of methods have been applied, including hydrothermal[4], solvothermal[5], sol–gel[6], solid state, microwave[7], precipitation[8], electrochemical oxidation[9], electrostatic deposition[10] or spin coating[11], to prepare Bi_2WO_6. Meanwhile, anodic oxidation of metallic foil has shown outstanding advantages in specific applications. Indeed, it allows for the formation of well-organized nanostructures with precisely controlled dimensions. It removes the step of a thin film preparation by powder deposition on a conductive substrate and, in turn, reveals the formation of stable materials[12]. Besides, thin film photocatalysts can be easily separated after photocatalytic reaction and recycled when compared to powder [13].

The low quantum yield, hence the limited application of Bi_2WO_6 is due to insufficient charge separation and consequently relatively fast recombination of charge carriers between the Bi6s and O2p orbitals and the empty W5d orbital. Thereby, numerous strategies have been proposed to enhance the photocatalytic performance (*e.g.,* morphology control, surface, and structure modification)[1]. Among these methods, the coupling of two semiconductors in heterojunction has gained great attention since it was found that it can promote a separation of electron-hole pairs through the closely contacted interfaces with the internal electric field and further improvement of the photocatalytic properties [14]. Additionally, heterojunction photocatalysts were found to possess higher photocatalytic activity than single-component photocatalysts in

* Corresponding authors.
E-mail addresses: anna.pancielejko@pg.edu.pl (A. Pancielejko), pawel.mazierski@ug.edu.pl (P. Mazierski).

https://doi.org/10.1016/j.apsusc.2021.151082
Received 1 July 2021; Received in revised form 23 August 2021; Accepted 23 August 2021
Available online 25 August 2021

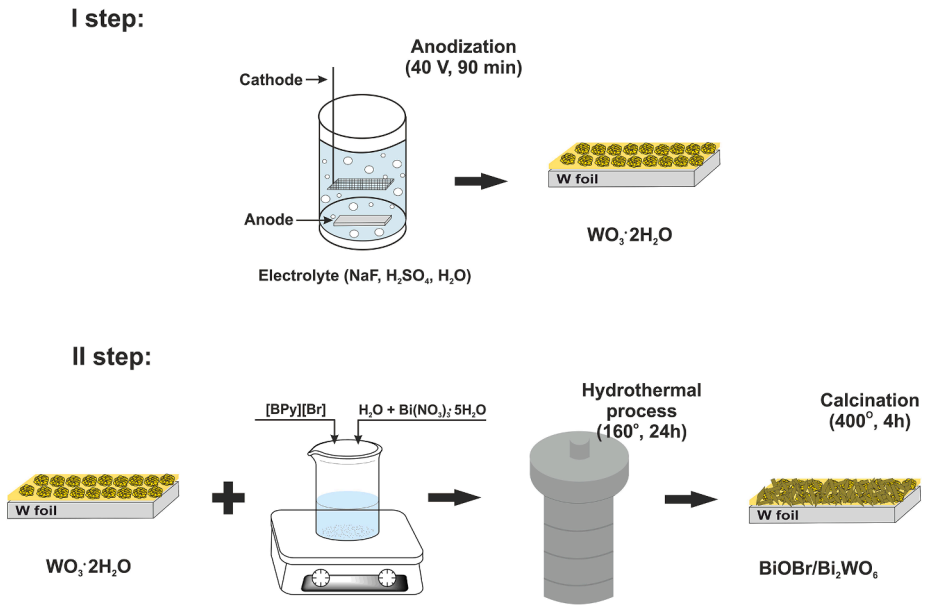

Fig. 1. Schematic diagram of the BiOBr/Bi_2WO_6 composite fabrication.

various photocatalytic applications in the Vis light region, *e.g.,* production of hydrogen and hydrocarbon fuels as well as degradation of organic pollutants[15–17]. Different photocatalysts with relatively high photocatalytic activity have been proposed for coupling with Bi_2WO_6, including Bi_2O_3[18], $BiVO_4$[19], bismuth oxyhalides BiOX (X = Br, Cl, I) [20], $Bi_2O_2CO_3$[21], *etc*. Bismuth oxyhalides are considered as promising materials due to their layered structure ($[Bi_2O_2]^{2+}$ layers and $[X]^-$ plates connected by Van der Waals interactions)[22]. The aforementioned structure determines good electron mobility and internal electric field, which results in the support of the separation of photogenerated charge carriers[22]. Among them, bismuth oxybromide (BiOBr) was found to be the most photocatalytically efficient structure due to the p-type indirect band gap, which is 2.6–2.9 eV[20].

Recently, ionic liquids (ILs) have been considered as promising template agents and source of halogens for the preparation of BiOX photocatalysts[23]. The importance of ILs has been appreciated due to their unique properties such as negligibly vapour pressure, low interfacial tension, high conductivity, and thermal stability[24]. From a practical point of view, the application of ILs could result in the synthesis of micro- and nanostructures with enhanced photocatalytic activity under visible light irradiation[25,26]. The mechanism of the improved photocatalytic reactions can be the result of the following factors: the nonmetal elements doping(N, F, or B) originated from IL into the photocatalyst structure, charge transfer or/and the formation of oxygen vacancies which could act as electron-trapping centres[27,28]. Up to now, the most commonly applied ILs for the synthesis of BiOX were imidazolium based ILs due to superior properties such as high thermal and electrochemical stability[29,30]. As far as we know, there is only one report in which pyridinium based IL was used for BiOX preparation [31]. Meanwhile, most works focused on the preparation of BiOBr/Bi_2WO_6 with KBr[32–34] while less is known about the effects of ILs on the morphology, photoelectrochemical and photocatalytic properties of BiOBr/Bi_2WO_6 heterojunction[35–37]. The methods used so far have led to the synthesis of BiOBr/Bi_2WO_6 powder composites, the main problems are low stability and difficulties with separation after photocatalytic reaction and recycle. Therefore, we propose a new technique for the direct two-step synthesis of BiOBr/Bi_2WO_6 heterojunction on the metallic foil in the presence of pyridinium-based IL towards degradation of organic environmental pollutants.

In this regard, we present, for the first time a novel approach to the BiOBr/Bi_2WO_6 thin film synthesis using N-butylpyridinium bromide [BPy][Br]. The preparation strategy involved two-step synthesis, first anodization of tungsten foil[38] and second, hydrothermal treatment of the as-anodized WO_3•$2H_2O$ in the presence of bismuth precursor and IL. The introduced IL served as a bromide ion source leading to the growth of BiOBr plates and allowed for a contact between BiOBr and Bi_2WO_6 in the heterojunction. This new strategy replaces the needs of powder deposition on a solid substrate, thus enabling its direct application. The IL-assistance synthesis of BiOBr/Bi_2WO_6 was found to improve the visible light absorption ability and enhance the phenol degradation, a model contaminant in water. The application of equimolar KBr instead of IL made it difficult to form p-n heterojunctions with similar reaction yield. For determining mechanism of the photocatalytic reactions, the analysis of the reactive oxygen species formation using benzoquinone, silver nitrate, ammonium oxalate, and *tert*-butanol as scavengers was performed. Additionally, action spectra measurements were carried out employing phenol solution.

2. Experimental Section

2.1. Materials

All reagents were of analytical purity and used without further purification. Isopropanol (p.a., POCh. S.A., Poland), acetone, methanol (p. a., P.P.H. STANLAB, Poland), and deionized water (DI, with conductivity of 0.05 μS) were used during the sonication process. Tungsten foil (0.127 mm, ≥99.9% purity, Sigma Aldrich, Germany), bismuth nitrate pentahydrate ($Bi(NO_3)_3$•$5H_2O$, ≥98.0% purity, Sigma Aldrich, Germany), sulphuric acid solution (96%, p. a., P.P.H. STANLAB, Lublin, Poland) and sodium fluoride (p. a., P.P.H. STANLAB, Lublin, Poland), N-butylpyridinium bromide [BPy][Br] (purveyed to ≥ 99.0% of purity, Iolitec, Germany) have been applied during the synthesis.

2.2. Preparation of BiOBr/Bi_2WO_6 heterojunction

Tungsten foils, cut into 2 × 2 cm^2 samples, were washed in acetone, isopropanol, methanol, and deionised water by sonication (10 min in each solvent). Afterwards, the samples were dried in an air stream[38]. The experiments were performed in a two-electrode system in which the as-cleaned foil was used as the working electrode and the platinum mesh as the counter electrode. Anodization was carried out in an electrolyte composed of sulphuric acid solution (1.0 M H_2SO_4) and sodium fluoride

(0.5 wt% NaF) for 90 min at a voltage of 40 V. As we reported previously, such kind of synthesis parameters established the photocatalyst with the most developed flower-like morphology and photocatalytic performance[38]. Meanwhile, $Bi(NO_3)_3{\bullet}5H_2O$ was dissolved in deionized water (120 mL), put under sonication (10 min) followed by intensive magnetic stirring (30 min) to end the reaction. Then, [BPy][Br] was added to the solution and still stirred (10 min). To investigate the effect of IL in the reaction mixture on the $BiOBr/Bi_2WO_6$ heterojunction properties, the molar ratio of IL to $Bi(NO_3)_3{\bullet}5H_2O$ was variable and ranged from 1:1, 1:4, 1:10 to 1:20 (while the amount of $Bi(NO_3)_3{\bullet}5H_2O$ was constant and equalled 20 mmol). Then, the as-anodized $WO_3{\bullet}2H_2O$ was placed on the bottom of the reaction vessel, filled with the solution of $Bi(NO_3)_3{\bullet}5H_2O$ and [BPy][Br], put in a Teflon-lined stainless steel autoclave and kept at 160 °C for 24 h. After cooling to room temperature, the as-prepared thin film was collected and rinsed with deionized water, dried overnight at 60 °C and then annealed at 400 °C (in an air environment, heating rate of 2 °C/min) for 4 h. Finally, the samples were allowed to cool down back to ambient conditions. Schematic diagram illustrating the synthesis procedure of $BiOBr/Bi_2WO_6$ composites is shown in Fig. 1. For comparison, the synthesis of $BiOBr\_KBr/Bi_2WO_6\_1$ composite with KBr instead of [BPy][Br] in molar ratio 1:1, while keeping other parameters unchanged, was performed. The pristine Bi_2WO_6 sample was synthesized without any addition of IL or KBr with similar conditions of anodization, hydrothermal synthesis, and calcination. Pristine BiOBr sample was prepared using ultrasonically washed W foil and the mixture of $Bi(NO_3)_3{\bullet}5H_2O$ and [BPy][Br] (in molar ratio 1:1), without anodic oxidation, with the same conditions of hydrothermal step and calcination.

2.3. Methods

Morphology of the obtained samples was analysed by high-resolution scanning electron microscopy (HRSEM, JEOL, JSM-7610F). To determine the thickness of the prepared films cross-sectional images were taken. The X-Ray diffraction (XRD) method was used to verify the crystal structure of the samples using a RigakuMiniFlex 600 system equipped with Cu Kα target. The average crystallite size was estimated using the Scherrer formula. The absorption spectra were recorded on UV–Vis spectrophotometer (Evolution 220, Thermo Scientific) equipped with an integrating sphere. The photoluminescence (PL) spectra were collected using a LS-50B photoluminescence spectrophotometer with 300 nm excitation wavelength at room temperature. Fourier-transform infrared spectroscopy (FTIR) was used to collect spectra with ATR accessories and a resolution of 8 cm^{-1} at room temperature by using a Nicolet iS10 FTIR (Thermo Fisher Scientific) spectrometer. Raman spectra were taken at room temperature using a Thermo Scientific DXR Smart Raman spectrometer with a 532 nm laser as the excitation source. The high-resolution (HR) XPS spectra were recorded for examining the chemical state of the elements present on the surface of the selected samples. The high-resolution (HR) XPS spectra were recorded on a PHI 5000 Versa Probe (ULVAC-PHI, Chigasaki Japan) scanning spectrometer using monochromatic Al K_α X-rays working with power 25 W. X-ray beam was focused to a diameter 100 μm and the measured area was defined as 500 × 500 μm. Binding energies (BE) of all detected XPS peaks were referenced to the C1s core level (BE = 284.8 eV).

2.4. Photocatalytic experiments

The photocatalytic activity was determined in two model processes: degradation of aqueous phenol solution and reactive oxygen species generation using benzoquinone, silver nitrate, ammonium oxalate and *tert*-butanol as scavengers under visible irradiation (λ > 420 nm). Additionally, action spectra analysis was performed to calculate the quantum efficiency of the phenol photooxidation under monochromatic irradiation.

2.4.1. Phenol decomposition

The experiments were performed in a quartz photoreactor filled with phenol (20 mg/L, 8 mL) and the sample in the middle. As the irradiation source, a 1000 W Xenon lamp (Oriel 66021), with an optical filter λ > 420 nm was used. The suspension was stirred (450 rpm) at first in the dark to achieve adsorption–desorption equilibrium for 30 min and then under visible irradiation for 240 min. Reference phenol samples (0.5 mL) were collected just before starting the analysis and subsequent samples were collected at regular time periods of 30 min during the irradiation process. The efficiency of the phenol degradation and the concentration of its intermediate's products were investigated by high performance liquid chromatography (HPLC, Shimadzu) analysis equipped with the SPD-M20A diode array detector operated at 225 and 254 nm, respectively.

2.4.2. Photocurrent measurements

Photocurrent measurements were carried out by an AutoLab PGSTAT 204 potentionstat–galvanostat with the standard three-electrode system with the prepared thin film composites as working electrode, while Ag/AgCl/3 M KCl and Pt mesh as the reference and counter electrodes, respectively. The active surface area of the working electrode was 0.25 cm^2. The electrolyte, 0.5 M Na_2SO_4, was purged with argon for 1 h before the experiments. The space above the electrolyte during the experiments was purged with argon also. Photocurrent measurements were taken under visible irradiation using a 250 W Xenon light source with a 420 nm cut-off filter.

2.4.3. Reactive oxygen species generation

To determine the role of active species generated during photocatalytic processes, the experiments were carried out in the presence of scavengers, namely, silver nitrate, ammonium oxalate, benzoquinone and *tert*-butyl alcohol of e^-, h^+, $^{\bullet}O_2^-$ and •OH radicals, respectively. The analysis was performed over aqueous solution containing phenol and the abovementioned scavengers (20 mg/L, 1:1 v/v). Besides, the experimental strategy was similar to that described in Section 2.4.1.

2.4.4. Action spectra measurements

Action spectra (AS) experiments were conducted for the most photoactive sample for the decomposition of phenol under monochromatic irradiation using a diffraction grating illuminator (Jasco, RM-FD) equipped with a 300 W Xenon lamp (Hamamatsu, C2578-02). The sample was placed in a cell made of quartz and filled with phenol solution (20 mg/L, 10 mL) and then irradiated at monochromatic wavelengths for 360 min (λ = 380, 400, 420, 440 and 460 nm) with continuously magnetic stirring. For comparison, reference samples of pristine BiOBr and Bi_2WO_6 were irradiated at a monochromatic wavelength of 420 nm for 360 min. The irradiation intensity was measured using an optical power meter (HIOKI 3664). During the photocatalytic process, every 60 min, the sample of the reaction mixture was taken with a syringe and analysed by HPLC. The apparent quantum efficiency (AQE) was determined as the ratio of the number of reacted electrons to the number of incident photons in accordance with the reaction stoichiometry in which two photons are required.

3. Results and discussion

Firstly, the $WO_3{\bullet}2H_2O$ thin film was obtained by an anodic oxidation of W foil in the acidic electrolyte containing fluoride ions under unstirred conditions. The SEM analysis revealed the growth of flower-like $WO_3{\cdot}2H_2O$ morphology with regular in shape and repeatable distribution of flower buds (Fig. S1). Secondly, the as-anodized sample was placed at the bottom of the Teflon-lined autoclave, filled with aqueous solution of bismuth precursor and [BPy][Br], hydrothermal treated, dried and finally calcinated. To determine the role of IL in BiOBr growth, a series of $BiOBr/Bi_2WO_6$ composites was prepared in the presence of [BPy][Br] or KBr. In addition, pristine BiOBr and Bi_2WO_6 were

Table 1
Sample code, molar ratio of IL or KBr to Bi precursor, average crystallite size, and diffraction peak intensity.

Sample code	Molar ratio of IL to Bi precursor	Molar ratio of KBr to Bi precursor	Average crystallite size (nm)		Diffraction peak intensity (a. u.)	
			Bi_2WO_6 (112)	BiOBr (102)	Bi_2WO_6 (112)	BiOBr (102)
Bi_2WO_6	–	–	9.4	–	6485	–
BiOBr/Bi_2WO_6_20	1:20		8.9	8.5	3785	294
BiOBr/Bi_2WO_6_10	1:10		32.4	16.3	1076	433
BiOBr/Bi_2WO_6_4	1:4		21.2	19.8	397	481
BiOBr/Bi_2WO_6_1	1:1		19.8	28.9	44	2453
BiOBr	1:1		–	27.9	–	2472
BiOBr_KBr/Bi_2WO_6_1	–	1:1	9.8	6.6	2302	473

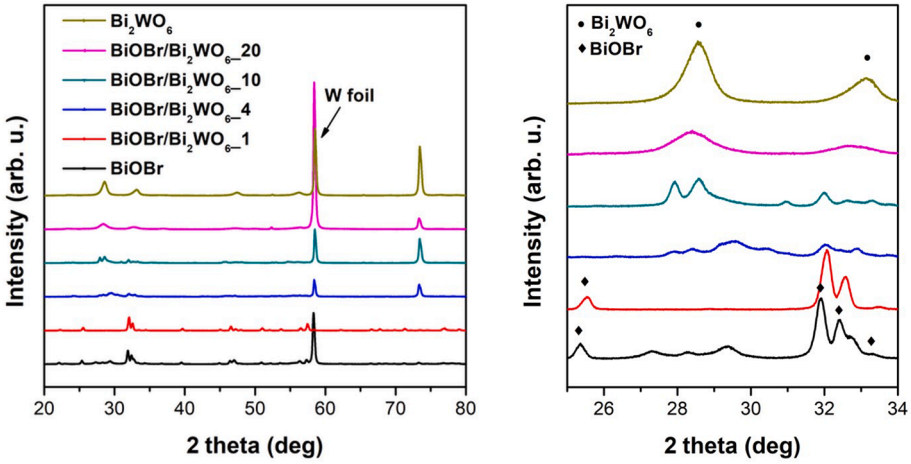

Fig. 2. XRD patterns of Bi_2WO_6, BiOBr/Bi_2WO_6 composites, and BiOBr.

prepared. Schematic diagram for the fabrication of the BiOBr/Bi_2WO_6 composite and a description are shown in Fig. 1 and Table 1, respectively. The sample's code, molar ratios of IL or KBr to the Bi precursor used during the synthesis, average crystallite sizes, and intensity of XRD diffraction peaks ascribed to BiOBr and Bi_2WO_6 were collected in Table 1. The photocatalysts were characterized taking into account structure, morphology, optical, and photoelectrochemical properties. Finally, the photocatalytic performance in the phenol degradation reaction accompanied by oxygen active species formation under visible light and phenol degradation as a function of irradiation wavelength to determine the range of the composite activity during the photocatalytic process were examined.

3.1. Photocatalysts characterization

To identify the crystalline structure of pristine BiOBr and Bi_2WO_6 photocatalysts as well as BiOBr/Bi_2WO_6 composites X-ray diffraction analysis was performed. The XRD patterns are shown in Fig. 2. In addition, the XRD investigation of the samples obtained subsequently after W foil anodization and hydrothermal treatment without IL or KBr assistance are shown in Fig. S2. The study revealed the formation of the characteristic peaks located at 2θ angles 13.1°, 24.4°, 26.1°, and 27.6° attributed to the (010), (200), (020) and (131) crystal planes of triclinic WO_3•$2H_2O$ (JCPDS card No. 1004057). The diffraction signals for pristine Bi_2WO_6 were observed at 2θ angles 28.58°, 33.17°, 36.82°, 47.55°, 56.29°, 73.41° and 76.29° corresponding to the (112), (200), (202), (204), (215), (411) and (316) crystal planes of tetragonal Bi_2WO_6 crystal (JCPDS card No. 1011215), respectively. The distinct diffraction peaks detected at 2θ angles 22.08°, 25.34°, 31.88°, 32.34°, 33.30°, 39.47°, 44.87°, 46.36°, 46.99°, 51.88°, 57.31°, 58.28°, 73.26° and 76.78° were attributed to the (002), (101), (102), (110), (003), (112), (004), (200), (113), (202), (212), (203), (301) and (205) crystal planes which indicated the presence of tetragonal BiOBr phase (JCPDS card No. 9009161), respectively. The crystal structure of both BiOBr and Bi_2WO_6 was gained following hydrothermal transformation prior to calcination. The annealing process was introduced to improve the crystallinity of the sample and to remove impurities remaining on the surface of the photocatalysts after synthesis, which decompose at an increased temperature. With increasing the BiOBr content, the peak's intensity of Bi_2WO_6 pattern gradually decreased with the arising of the diffraction peaks indexed to BiOBr crystal phase (see Fig. 2 and Table 1). It could be due to the p-n heterojunction formation in which BiOBr and Bi_2WO_6 competed for the place. In contrast, it was hard to establish typical patterns of BiOBr in BiOBr/Bi_2WO_6_20 as a result of a very low BiOBr content corresponding to the very low amount of IL used during the synthesis (Fig. 2 and Table 1). The peak detected at 2θ angle approx. 58.57°, originating from the W foil, was observed in all samples beside BiOBr/Bi_2WO_6_1 probably due to the higher denser coverage of the Bi_2WO_6 surface with BiOBr. In addition, the analysis of the sample prepared in the equimolar KBr instead of [BPy][Br], BiOBr_KBr/Bi_2WO_6_1, revealed a very low intensity of the peaks ascribed to BiOBr and Bi_2WO_6 phases confirming the significant role of IL in the heterojunction formation (Fig. S3).

Average crystallite sizes were estimated from the Scherrer equation and the results are presented in Table 1. The crystallite sizes of pristine Bi_2WO_6 and BiOBr were equalled to 9.4 and 27.9 nm, respectively. A linear increase of the BiOBr crystallite size was detected when a higher amount of IL was used during hydrothermal treatment (from 8.5 to 28.9 nm for BiOBr/Bi_2WO_6_20 and BiOBr/Bi_2WO_6_1, respectively) while the crystallite size of Bi_2WO_6 decreased (except BiOBr/Bi_2WO_6_20, the values change from 32.4 to 19.8 nm, respectively). It could suggest that the crystallite sizes of BiOBr were higher and could cover the Bi_2WO_6 surface (Table 1). Notably, the crystallite sizes of Bi_2WO_6 and BiOBr in BiOBr_KBr/Bi_2WO_6 samples were estimated to be 9.8 and 6.6 nm. This decline of the crystallinity degree between the composites prepared in the presence of [BPy][Br] or KBr might be caused by some differences in

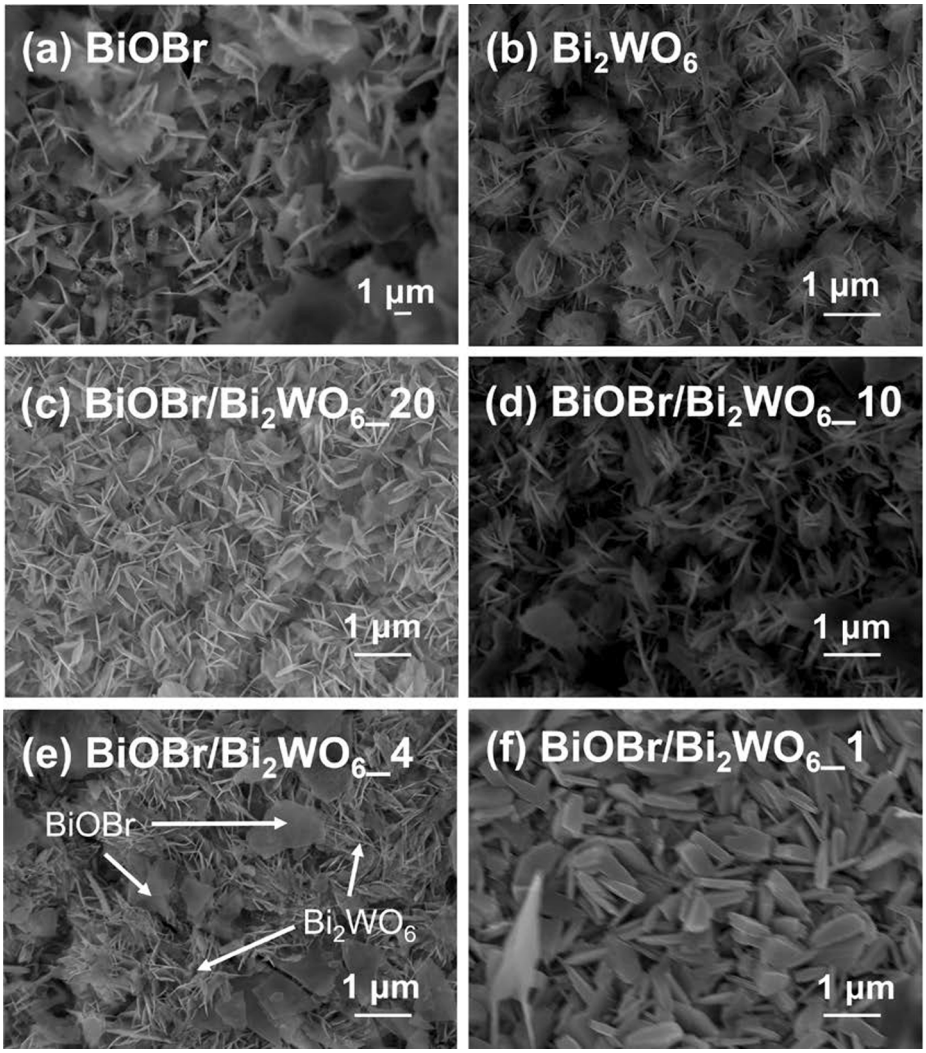

Fig. 3. SEM images of (a) BiOBr, (b) Bi_2WO_6, (c) BiOBr/Bi_2WO_6_20, (d) BiOBr/Bi_2WO_6_10, (e) BiOBr/Bi_2WO_6_4 and (f) BiOBr/Bi_2WO_6_1.

the formation process of BiOBr/Bi_2WO_6 depending on the Br^- source and will be further discussed.

The morphology of pristine Bi_2WO_6 and BiOBr as well as BiOBr/Bi_2WO_6 composite materials is shown in Fig. 3. Pristine BiOBr consisted of plates of irregular shape ranging from 1.5 ± 0.2 to 3 ± 0.35 μm (Fig. 3a). Pristine Bi_2WO_6 sample (Fig. 3b) exhibited an ordered, regular shape of a flower-like structure with the thickness and diameter equaling 1.1 ± 0.1 μm and 1.2 ± 0.1 μm, respectively. The flower-like structure was composed of plates clustered in the centre with the thickness of 14.9 ± 0.3 nm. The BiOBr/Bi_2WO_6_20 sample did not show the presence of BiOBr plates on the surface, which suggests that with such a small amount of IL used for synthesis, BiOBr was formed in a very low amount (Fig. 3c). Increase of the IL content used during the preparation resulted in an increase in the amount of BiOBr plates in the composite, which are shown in Fig. 3d and e, where individual plates of this material can be observed on the surface of Bi_2WO_6. These plates were of irregular shape with thickness reaching 13.5 ± 0.25 nm. For the sample with the highest BiOBr content (BiOBr/Bi_2WO_6_1), it was observed that the entire surface of Bi_2WO_6 was completely covered with irregular, thick plates of BiOBr (Fig. 3f). The formation of BiOBr plates occurred on the flower-like structure, creating a morphology similar to the core (Bi_2WO_6)-shell (BiOBr) structure and creating growth sites for larger plates of BiOBr (with higher IL content). Thus, the resulted Bi_2WO_6 flower-like surface was covered by BiOBr plates with good adhesion.

Taking into consideration the above presented results, the formation process of the BiOBr/Bi_2WO_6 heterojunction was suggested. The first synthesis step, anodic oxidation of W foil in the electrolyte composed of sulphuric acid solution (1.0 M H_2SO_4) and sodium fluoride (0.5 wt% NaF), resulted in the growth of the self-assembled flower-like WO_3•$2H_2O$ structure, as we reported previously (Fig. S1)[38]. In short, the process involved (i) pore formation, (ii) dissolution of the oxide layer by the F^- ions activation, and the final stage led to (iii) deepening and increase of the thickness of flower-like layer of tungsten (VI) oxide. Application of the electrochemical method allowed for the synthesis of the WO_3•$2H_2O$ thin film with a flower-like morphology, which was preserved later during the hydrothermal synthesis into Bi_2WO_6. Second step concerned the transformation of the as-anodized WO_3•$2H_2O$ into Bi_2WO_6 or BiOBr/Bi_2WO_6 composite in the presence of [BPy][Br]. For this purpose, the bismuth nitrate pentahydrate was hydrolysed with water to a white, bismuth oxynitrate ($BiONO_3$), consisting $[Bi_2O_2]^{2+}$ layer structure, according to the following equation:[39]

$$Bi(NO_3)_3 \bullet H_2O \rightarrow BiONO_3 + 2HNO_3 + 4H_2O$$

The formation of Bi_2WO_6 could be attributed to a substitution of a water molecule in the as-anodized WO_3·$2H_2O$ layer structure with $[Bi_2O_2]^{2+}$ layers during the hydrothermal step[9]. Upon addition of [BPy][Br], the reaction of $BiONO_3$ resulted in the slow formation of Bi^{3+}-IL complex. It could be suggested that the strong coordination interaction between [BPy][Br] and Bi^{3+} would slow the release rate of Bi^{3+} realised from $BiNO_3$, thus the reaction of BiOBr formation. The

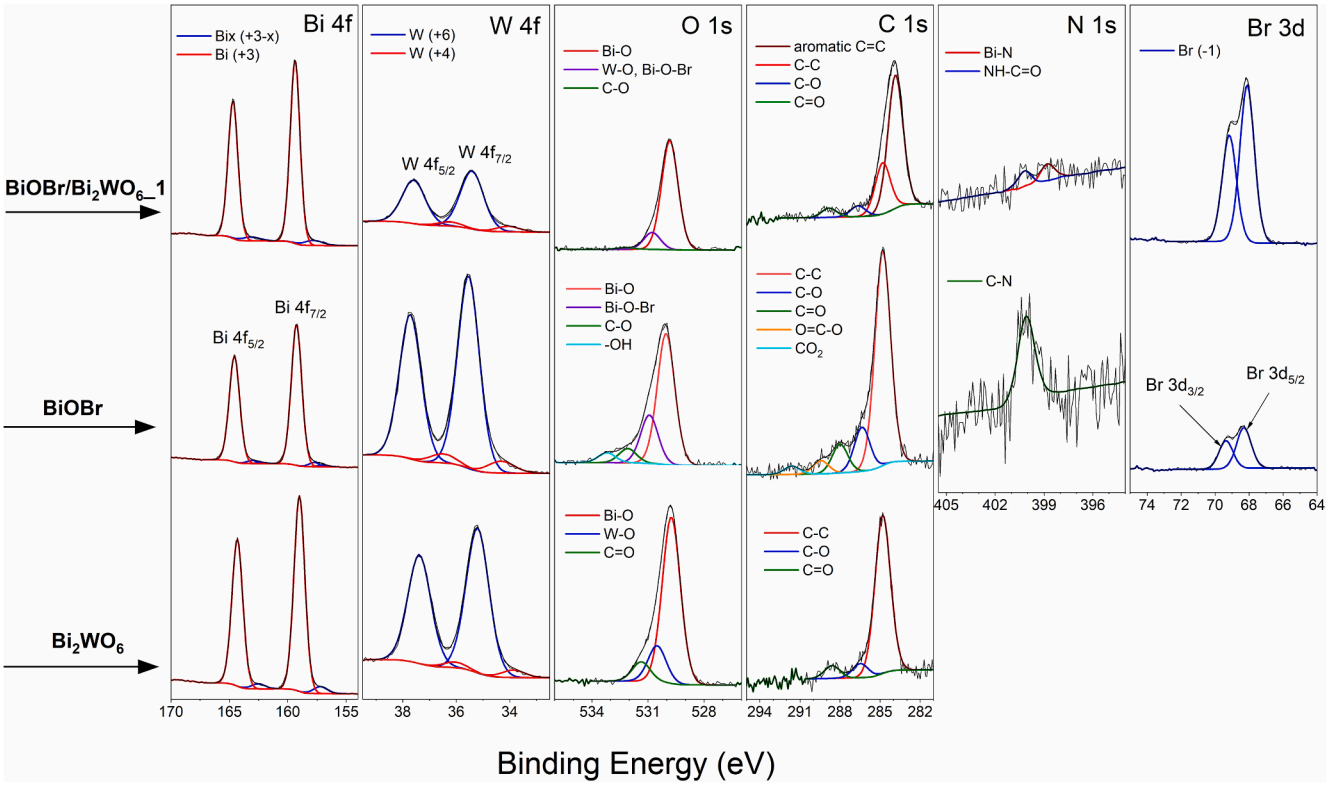

Fig. 4. High resolution Bi4f, W4f, O1s, C1s, N1s, and Br3d XPS spectra recorded on $BiOBr/Bi_2WO_6$_1, BiOBr, and Bi_2WO_6 photocatalysts.

coordination interaction existing between IL and Bi^{3+} will be further discussed. Meanwhile, the addition of KBr salt of strong acid and strong basic resulted in the immediate formation of a yellow precipitate of $BiBr_3$ which was further hydrolysed to BiOBr. Differences in the structure of the samples obtained in the presence of IL and KBr may be related to the different solvation of the ions forming these salts in the reaction medium. The process of BiOBr growth might occur as a dissolution recrystallization process and led to covering of the Bi_2WO_6 surface with the BiOBr plates.

The elemental composition and characteristics of the elements detected in the surface area of the selected Bi_2WO_6, BiOBr, and $BiOBr/Bi_2WO_6$_1 photocatalysts were examined by XPS. The elemental composition is specified in Table S1 and the chemical states of Bi, W, O, C, N, and Br, detected in these samples were identified by deconvolution of the corresponding Bi4f, W4f, O1s, C1s and Br3d HR spectra (see description of deconvoluted states in Fig. 4). The Bi4f spectra of all samples consisted of two states, Bi(+3) and Bi(+3-x), represented by Bi $4f_{7/2}$ signals at 159.1 and 157.2–157.8 eV, respectively[40–43] (Table S1). The W $4f_{7/2}$ signals at 35.4 and 34.1 ± 0.2 eV showed the coexistence of the main W(+6) oxidation state and a small contribution of W(+4), respectively [40]. Both signals identified Bi_2WO_6 component [40–42]. The O1s feature of $BiOBr/Bi_2WO_6$_1 was similar to that of Bi_2WO_6 and BiOBr composites. The peaks positioned at 529.8, 530.8, and 532.2 eV can be assigned to Bi-O, Bi-W/Bi-O-Br, and C-O bonds [41,44]. The C1s spectrum of $BiOBr/Bi_2WO_6$ was resolved into four components, placed at 283.9, 284.8, 286.6, and 288.8 eV, respectively. The lowest BE component is attributed to C = C aromatic carbon bound [45], confirming the effective interaction of [BPy][Br] IL with $BiOBr/Bi_2WO_6$. The latter peaks are usually assigned to C-C, C-O, and C = O carbon bonds, respectively[40,45,46]. The presence of IL species in the surface area of $BiOBr/Bi_2WO_6$_1 composite was also confirmed from N1s and Br 3d spectra. Two N1s peaks were observed at BE of 399.3 and

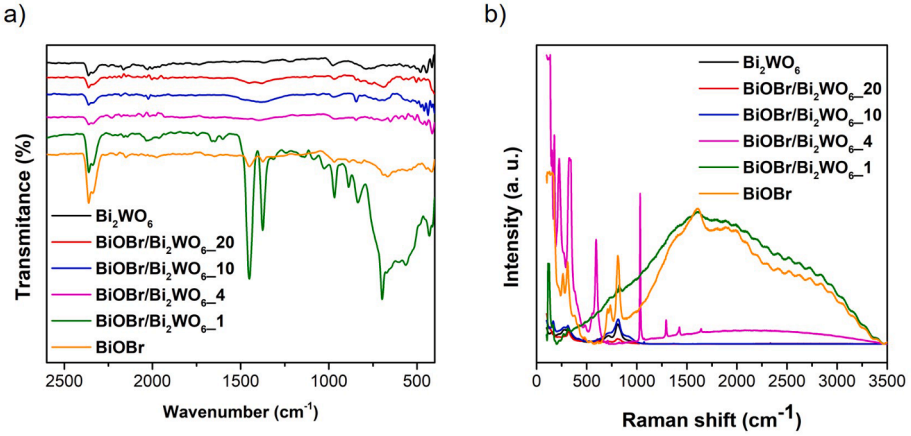

Fig. 5. (a) FTIR and (b) Raman spectra of Bi_2WO_6, $BiOBr/Bi_2WO_6$, and BiOBr photocatalysts.

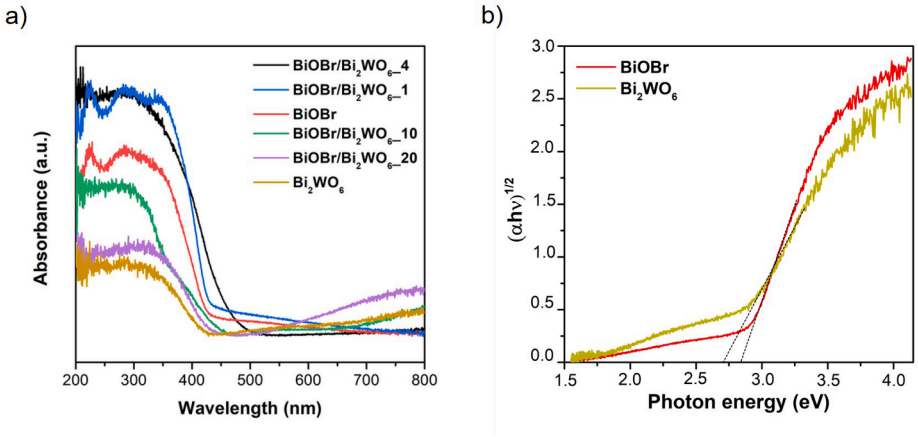

Fig. 6. Normalized (a) UV–Vis diffuse reflectance spectra of Bi_2WO_6, BiOBr/Bi_2WO_6, and BiOBr samples and (b) Tauc plot of Kubelka Munk (K-M) curves of pristine Bi_2WO_6 and BiOBr.

400.7 eV, which are ascribed to Bi-N [42,46,47] and NH-C = O bounds [48], respectively. Formation of Bi-N bounds can be the result of partial decomposition of IL and the interaction of N atoms with BiOBr/Bi_2WO_6. The Br3d spectra (Br $3d_{5/2}$ located at 68.1 eV) originated from BiOBr [44] and from IL. However, the surface content of Br, expressed as the Br/Bi atomic ratio, was much higher in the BiOBr/Bi_2WO_6 than in the BiOBr photocatalyst (Table S1). Thus, most of Br atoms in BiOBr/Bi_2WO_6_1 composite was probably derived from [BPy][Br] IL.

The FTIR spectroscopy was employed to confirm the coupling of BiOBr and Bi_2WO_6 as well as the presence of functional groups (Fig. 5a). Additionally, the spectrum of pristine [BPy][Br] was performed as shown in Fig. S4. The peaks of pristine photocatalysts, BiOBr and Bi_2WO_6, were in accordance with the previously reported results[49]. The spectra revealed the bands corresponding to Bi-O stretching, W–O stretching, and W–O–W bridging stretching modes in the range of 400–1000 cm^{-1}[50]. The absorption peaks above 1000 cm^{-1} revealed the presence of various functional groups, such as C = C stretching vibration of the IL's heterocyclic ring and –OH bending vibration (1640 cm^{-1}) attributed to the adsorbed water. Comparing the spectra of the composites, it was found that they possessed similar peak features, however, intensity of the signals corresponding to Bi-O-Br vibration decreased with lower BiOBr content. The appearance of a broad spectrum of [BPy][Br] in the range of 400–4000 cm^{-1} confirmed the presence of some IL residues in the composite's spectra (especially noticeable in the BiOBr/Bi_2WO_6_1 spectrum). Indeed, the absorptions caused by ring vibration presence appeared near 980, 890, 840, and 690 cm^{-1}, while the signals at 2360–2150 cm^{-1} could be attributed to the vibration of C = N.

To investigate the chemical structure and interaction between pristine BiOBr and Bi_2WO_6 and their composites, the Raman spectra were collected (Fig. 5b). Analysis of pristine Bi_2WO_6 revealed the presence of several peaks located in 147, 162, 279, 309, 422, 721, and 824 cm^{-1}. The bands located in 147, 162, 215, 279, 309, and 422 cm^{-1} could be caused by the bending vibrations of the WO_6 octahedral. The band of 289 cm^{-1} could be ascribed to the translational modes of simultaneous motion of Bi^{3+} and WO_6^{2-}. The peak of 721 cm^{-1} could be assigned to the antisymmetric bridging modes of WO_6 octahedral[51]. The band at 824 cm^{-1} could correspond to the symmetric and antisymmetric modes of O-W-O[52]. The Raman spectra of BiOBr/Bi_2WO_6 composites included peaks corresponding to both Bi_2WO_6 and BiOBr, depending on the BiOBr amount. Actually, the characteristic Raman peaks of BiOBr were easily to distinguish in the spectra of BiOBr/Bi_2WO_6_4, which consisted of bands located in 135, 385, 479, 547, and 714 cm^{-1}. With increasing BiOBr content, the characteristic peaks of Bi_2WO_6 disappeared probably due to the covering in the highest extent the Bi_2WO_6 surface with BiOBr. Some shifts of the bands might occur because of differences in crystallinity and structure.

UV–Vis diffuse reflectance absorption spectra (UV–Vis DRS) of the as-prepared photocatalysts provided essential details about their ability to reflect irradiation and band gap positions, and thus, their photoactivity (Fig. 6a and b). According to the obtained results, BiOBr photocatalyst exhibited photoresponse properties from the UV region to visible light until 425 nm, while Bi_2WO_6 has shown strong visible light absorption. The light absorption abilities of the BiOBr/Bi_2WO_6 composites were red-shifted as a consequence of coupling those photocatalysts[53]. The increase amount of BiOBr resulted in weaker visible light absorption due to the cover of increasingly Bi_2WO_6 surface, which could cause a light shielding effect. However, the nonlinear changes of the absorption edges were observed. It was considered that if a small fraction of the BiOBr covered the Bi_2WO_6 surface, the absorption ability would have varied independently and an estimation of the electric state of the prepared composites could be adulterated. Noticeable pristine Bi_2WO_6 as well as the composites with the lowest amount of BiOBr, BiOBr/Bi_2WO_6_20, and BiOBr/Bi_2WO_6_10, exhibited strong light absorption above 400 nm which could be attributed to a decrease in the amount of suboxides and oxygen vacancies. The band gap energies (E_g) of BiOBr and Bi_2WO_6 were estimated in accordance to Tauc plot as a function of the photon energy *vs.* $(\alpha h\nu)^{1/2}$(Fig. 6b) where α and hν are the absorption coefficient and the light frequency. The E_g were about 2.84 and 2.71 eV for BiOBr and Bi_2WO_6, respectively, in line with literature reports[20,54,55].

The PL measurements were used to investigate the migration, transport, and recombination process of the photogenerated charge carriers. To illustrate the efficiency of this phenomenon, the composites were excited by a 300 nm wavelength and the results are displayed in Fig. S5. It was found that all samples showed an apparent characteristic emission peak from 420 to 520 nm. The strong peak emission at approx. 420 nm might be ascribed to the intrinsic transition of Bi^{3+} ions from the 6 s 6p excited state to the 6 s2 ground state[56]. The strong emission peak found at 448 nm could be assigned to the intrinsic luminescence of Bi_2WO_6 photocatalyst related to the charge transport between the orbitals of Bi6s and O2p to the empty orbital in the WO_6^{2-} surface complex. Finally, the emitting peaks at approx. 479 and 529 nm might correspond to the surface defects caused by the presence of metal atoms and oxygen vacancies appeared during the growth process. The positions of the composites emission peaks were similar to those of pristine Bi_2WO_6 and might suggest a physical absorption as a result of the interaction between BiOBr and Bi_2WO_6[53]. The intensity of the PL BiOBr/Bi_2WO_6 bands decreased significantly as the BiOBr content decreased towards the spectrum of pristine Bi_2WO_6. It could suggest a reduction in the recombination rate of the charge carriers due to heterojunction formation. On the other hand, the stronger PL intensity

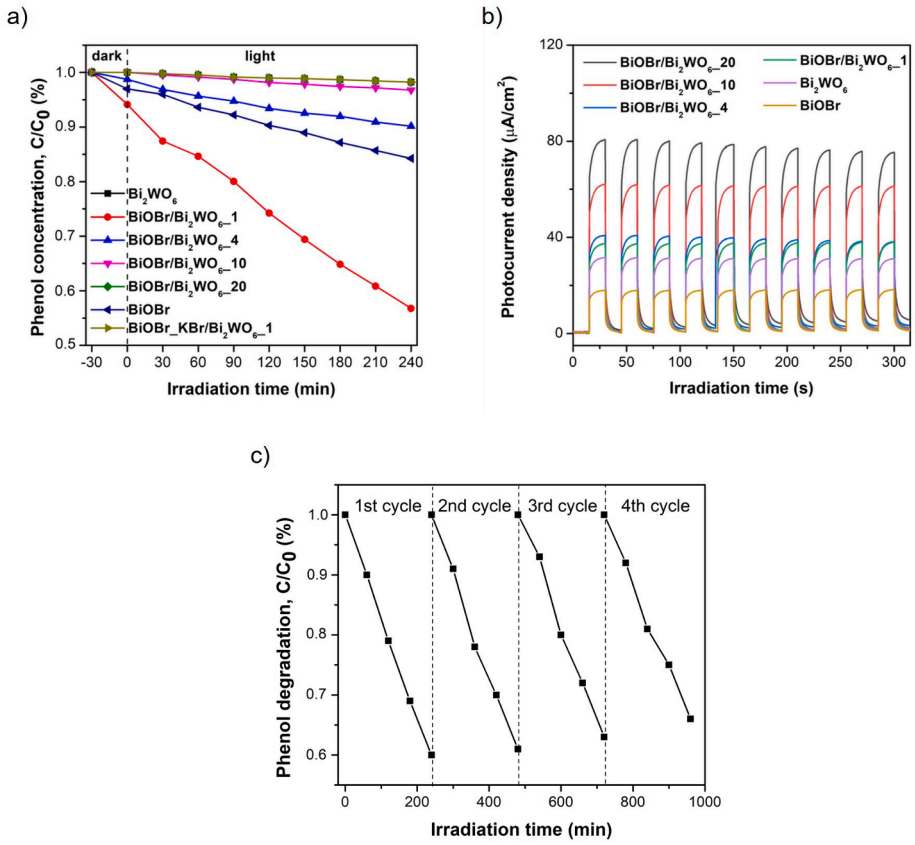

Fig. 7. (a) Photocatalytic decomposition of phenol, (b) photocurrent response registered at 1.0 V in 0.5 M Na_2SO_4, and (c) photostability of the most photoactive sample ($BiOBr/Bi_2WO_6$_1) in four consecutive cycles under visible irradiation (optical filter > 420 nm).

might suggest a higher oxygen vacancies concentration. The high electron effect of the oxygen vacancies can facilitate electrons photogeneration and thus, promotes the separation process of photogenerated carriers. However, too high oxygen vacancies concentration would become the recombination centre. Therefore, it was observed that with increasing BiOBr content in the composites, the PL intensity increased and reached the highest level in the case of pristine BiOBr.

3.2. Photocatalysts performance

The photocatalytic behaviours of the pristine photocatalysts and their composites were evaluated by observing decomposition of the aqueous phenol solution after 240 min of visible light irradiation ($\lambda >$ 420 nm.). The results are displayed in Fig. 7a. The blank test in the absence of photocatalysts resulted in a very low efficiency phenol degradation. The efficiency of the phenol adsorption in the dark for the series of the prepared samples were around of 6%. Evidently, the enhancement of photoactivity was attributed to the $BiOBr/Bi_2WO_6$ heterojunction construction, while pristine BiOBr and Bi_2WO_6 showed much lower activity, similar as it was earlier in other references[36,54]. Among all composite samples, $BiOBr/Bi_2WO_6$_1 showed the highest efficiency compared with pristine BiOBr and Bi_2WO_6 (3 times higher than that of BiOBr, while Bi_2WO_6 was negligibly photoactive under measured conditions). The photocatalytic activities of $BiOBr/Bi_2WO_6$_4, $BiOBr/Bi_2WO_6$_10, and $BiOBr/Bi_2WO_6$_20 decreased linearly with decreasing BiOBr content and were between that of BiOBr and Bi_2WO_6 (Fig. 7a). Meanwhile, the photoactivity of the $BiOBr_KBr/Bi_2WO_6$_1 composite was not detectable under visible irradiation. This could be because of the differences in the crystallinity and the formation of $BiOBr/Bi_2WO_6$ in the presence of IL and KBr (Table 1 and Fig. S3). As described above, the application of inorganic salt during the hydrothermal step led to the formation of heterojunction characterized by low crystallinity degree, while the employment of [BPy][Br] revealed the formation of the composite with a much higher degree (see Fig. S3). The heterojunction formation might promote (i) charge transport between BiOBr and Bi_2WO_6 and (ii) separation of the electron-hole pairs generated during the photooxidation process and thus, influence on the photocatalytic performance. Similar to us, Ren *et al.* also analysed the photoactivity of the powder Bi_2WO_6/BiOBr composite prepared with KBr or [C_{16}mim][Br] assistance and evidently realised that better photoactivity was ascribed to the positive effect of the IL presence[36]. Zhu *et al.* released that replacement of [BMIM][Cl] by KCl resulted in the formation of amorphous BiOCl in Bi_2WO_6/BiOCl heterojunction and further affected its low photocatalytic performance[57].

In addition, the photocatalytic degradation process in the presence of the most active sample, $BiOBr/Bi_2WO_6$_1 revealed the formation of benzoquinone and hydroquinone as the phenol decomposition intermediates products under visible irradiation. As revealed, the concentration of both of them initially increased and then began to decline (Table S2), implying a slow mineralization process of phenol.

Obtained samples were also studied in terms of their photoelectrochemical activity. Fig. 7b shows photocurrent measurements (chronoamperometry) in light off/on cycles at 1.0 V in 0.5 M Na_2SO_4. The switch on/off period was 30 s. For all studied samples, a negligible current was observed under dark conditions. When the irradiation was switched on, the current began to increase and stabilize after a few seconds. Pristine BiOBr and Bi_2WO_6 showed much lower photoelectroactivity, lower than any composite sample. The highest current response was noticed for $BiOBr/Bi_2WO_6$_20, almost 4 and 2.5 times higher compared to BiOBr and Bi_2WO_6, respectively, which was opposite to the results of the photocatalytic activity, where the most active composite was $BiOBr/Bi_2WO_6$_1. The lower BiOBr content in the

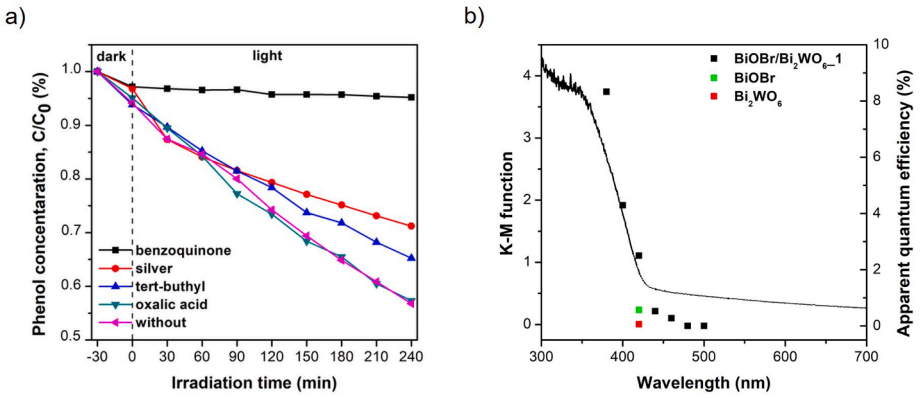

Fig. 8. (a) Degradation of phenol with and without scavengers under visible irradiation (optical filter > 420 nm) and (b) AS for phenol oxidation over BiOBr/Bi_2WO_6_ 1, BiOBr and Bi_2WO_6 (AQE – squares) *vs.* absorption spectrum of BiOBr/Bi_2WO_6_1 (K-M function – line).

composite, the higher photocurrent response was recorded, which is probably related to the different environment of carrying out these measurements, hence the different response of the composites. Obtained samples also showed good stability, measured in 10 measuring cycles with light off/on cycles (Fig. 7b). Noteworthy, these results were in line with the PL measurements (Fig. S5) and suggest more effective charge transfer and separation in the BiOBr/Bi_2WO_6_20 photocatalyst compared to the other composites. The excessive loading of BiOBr could hinder the light absorption of the composites. As revealed, the lower optical absorption efficiency at visible light range (above 400 nm) observed for the photocatalysts with higher BiOBr content resulted in lower photoelectrochemical performance. An increase of BiOBr content decreased the current response due to the hindering effect of large amount BiOBr nanoplates covered on the top surface of flower-like Bi_2WO_6.

Considering the practical application, the photostability of the most active composite, BiOBr/Bi_2WO_6_1 was examined in four subsequent cycles under the same conditions as the photoactivity measurements and the results are shown in Fig. 7c. The obtained values revealed a slight decrease of photoactivity (from 41 to 34% after 4 processes), suggesting that the BiOBr/Bi_2WO_6 composites prepared in the presence of IL changed only a bit during the irradiation process and could be recycled.

3.3. Discussion of the photocatalytic mechanism

To understand the role of active species involved in the photodegradation of phenol, trapping experiments were performed using BiOBr/Bi_2WO_6_1. Ammonium oxalate, silver nitrate, benzoquinone, and *tert*-butanol were used as scavengers of h^+, e^-, $^{\bullet}O_2^-$ and •OH, respectively. Reactive species experiments indicated that the addition of *tert*-butanol and silver nitrate did not affect on the phenol degradation, which suggested their minor role in the process (Fig. 8a). In addition, if ammonium oxalate was added to the reaction system, the efficiency of the reaction was also slightly decreased, implying that might be a second reactive species in this process. While, the addition of benzoquinone caused an inhibitory effect on the phenol degradation, indicating the crucial role of $^{\bullet}O_2^-$ in the photocatalytic phenol degradation under visible light irradiation. Although, the literature data have shown some differences in the mechanism of reactive species formation over BiOBr/Bi_2WO_6 heterojunction. For example, He *et al.* indicated that h^+ and $^{\bullet}O_2^-$active species were involved in the Rhodamine B degradation process[37]. In contrast, Ren *et al.* suggested that h^+ and •OH were mainly formed during the photocatalytic reaction of organic pollution photodegradation [36]. Wang *et al.* realised that h^+ were the major species in the photooxidation of benzyl alcohol in the presence of BiOX/Bi_2WO_6 (X = Cl, Br, I) while the role of hydroxyl and superoxide radicals was just a minor[20]. We assume that that difference in the mechanism of organic pollutants photooxidation might originate from the composite's synthesis route and further influence on the photocatalytic properties.

To exhaustively explore the photocatalytic mechanism of the BiOBr/Bi_2WO_6 heterojunction excitation under visible light, the phenol degradation was examined as a function of monochromatic irradiation to determine the equal range of the BiOBr/Bi_2WO_6_1 composite photoactivity. For comparison, the AS process was performed in the presence of pristine BiOBr and Bi_2WO_6 photocatalysts excited with a wavelength of 420 nm. The results for phenol photooxidation over BiOBr/Bi_2WO_6_1, BiOBr, and Bi_2WO_6 (AQE – squares) *vs.* the absorption spectrum of BiOBr/Bi_2WO_6_1 (K-M function – line) are shown in Fig. 8b. As can be observed, the excitation of the BiOBr/Bi_2WO_6_1 composite in the range of 380–460 nm caused the phenol degradation, whereas the pristine Bi_2WO_6 and BiOBr possessed negligible photocatalytic activity excited with a wavelength of 420 nm. Clearly, the apparent quantum efficiency (AQE) for the BiOBr/Bi_2WO_6 composite was significantly higher than that for the pristine photocatalysts (Fig. 8b). The AQE value of the BiOBr/Bi_2WO_6_1 sample (4.29%) was 8 and 71.5 times higher than that of the pristine BiOBr and Bi_2WO_6 photocatalysts (0.57 and 0.06%, respectively) after excitation with the wavelength of 420 nm.

According to the above results and discussion, it can be concluded that the establishment of the p-n heterojunction between BiOBr and Bi_2WO_6 in the presence of [BPy][Br] was crucial for the enhancement of photocatalytic activity of the composites, similar as the others reported previously[54,57–60]. Usually, in single-component BiOBr and Bi_2WO_6 photocatalysts, the photogenereated electron-hole pairs would rapidly recombine. However, the coupling of those two matchable semiconductors into heterojunction might slow down this process and improve the photoactivity (Fig. 7a). The appearance of N atoms on the surface of the photocatalysts originated from partial IL decomposition might be related to the decrease of the electron-hole pairs recombination rate (Table S1). Thus, we observed enhanced photoactivity of N-modified BiOBr and the corresponding BiOBr/Bi_2WO_6 material.

Further insight into the photocatalytic ability of the BiOBr/Bi_2WO_6 composite by analysis of the band gap positions of pristine BiOBr and Bi_2WO_6 was essential to fully understand the mechanism. The band potentials were estimated on the basis of the following statement:

$$E_{CB} = X - E_c - \frac{1}{2}E_g$$

$$E_{VB} = E_{CB} + E_g$$

$$X = \frac{1}{2}(E_A + E_{ion})$$

where E_{CB} is the conduction band edge potential (CB), E_{VB} is the valance band edge potential (VB), X is the electronegativity of the photocatalyst estimated on the basis of the absolute electronegativity

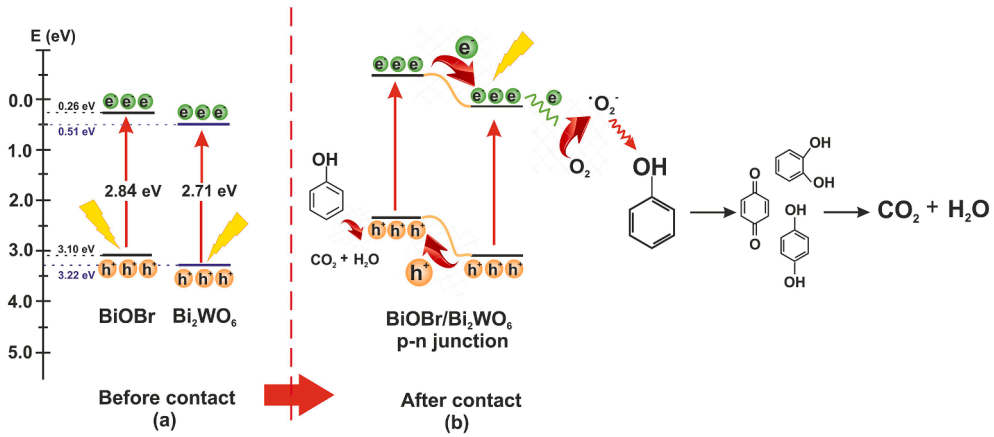

Fig. 9. (a) Schematic diagram of the energy positions of BiOBr and Bi_2WO_6 before contact and (b) possible photocatalytic mechanism of phenol degradation after p-n heterojunction formation under visible-light irradiation.

(E_A) and the first ionization energy (E_{ion}) of the constituent atoms (being 6.18 and 6.36 eV for BiOBr and Bi_2WO_6, respectively[36]). E_C is the energy of free electrons on the scale (4.5 eV). Based on the calculated E_g positions (Fig. 6b), the E_{CB} values of BiOBr and Bi_2WO_6 were equalled 0.26 and 0.51 eV, and their E_{VB} were 3.10 and 3.22 eV, respectively.

Taking into consideration the above presented results, a reasonable explanation of the heterojunction formation between BiOBr and Bi_2WO_6 could be proposed. Heterojunction formation has been confirmed by measuring Mott – Schottky, as shown in Figure S6, due to characteristic "V" shaped curve[61].The schematic diagram of the photocatalytic excitation mechanism over BiOBr/Bi_2WO_6 composite under visible irradiation is presented in Fig. 9. When BiOBr and Bi_2WO_6 were in contact, the Fermi level of BiOBr (p-type semiconductor) upshifted, whereas for Bi_2WO_6 (n-type semiconductor) a downward shift occurred until the equilibrium state was achieved[14,54]. As a result of an exposition to the visible light irradiation, the photogenerated electron-hole pairs were excited. Due to the interfacial potential gradient between those two photocatalysts, the photogenerated electrons were pushed from BiOBr surface towards the CB of Bi_2WO_6 and, at the same time, the holes from Bi_2WO_6 migrated to that of BiOBr. It was considered that the photoinduced holes might directly oxidize the phenol, and thus the high adsorption capacity was beneficial for its photocatalysis. The adsorbed organic molecules on the surface of the composite could be photosensitized by visible irradiation, and then a photogenerated electron was transported to CB where can be captured by O_2 to generate $^{\bullet}O_2^-$. The superoxide radicals were the main species involved in the photocatalytic reaction, while the participant of the hydroxyl radicals was negligible and could result from the $^{\bullet}O_2^-$ radicals.

4. Conclusions

The p-n BiOBr/Bi_2WO_6 heterojunction has been successfully prepared on the metallic foil through a novel two-step synthesis route using the ionic liquid, N-butylpyridinium bromide [BPy][Br], as Br^- source. A thin film of flower-like $WO_3 \cdot 2H_2O$, prepared by an electrochemical oxidation of W foil in an acidic solution containing F^- ions, was subsequently transformed into the BiOBr/Bi_2WO_6 heterojunction in the presence of [BPy][Br]. The formation of BiOBr plates occurred on the flower-like Bi_2WO_6 surface, creating a morphology similar to the core (Bi_2WO_6)-shell (BiOBr) structure and creating growth sites for larger plates of BiOBr (dependently on the IL content). In comparison, the replacement of the IL with the inorganic salt, KBr, made it difficult to form a heterojunction by using this method. For the first time, we described the application of BiOBr/Bi_2WO_6 thin film heterojunction for pollutant decomposition in an aqueous media using phenol as a model organic compound. The photocatalytic activity of the BiOBr/Bi_2WO_6 composites was closely related with BiOBr content as a result of IL amount used for the synthesis. The highest photoactivity was found for the BiOBr/Bi_2WO_6_1 photocatalyst (almost 3 times higher than that of BiOBr, while Bi_2WO_6 was not active under visible irradiation). Decrease of the IL amount used during the synthesis resulted in lower BiOBr formation and further affected on the linear decrease of the photocatalytic performance. The enhancement photoactivity originated from (i) the interactions of bromide ions, (ii) nitrogen incorporation into BiOBr structure originated from partially decomposed IL, and (iii) the close interface contact between BiOBr and Bi_2WO_6 with matchable energy band gap positions, which improved the efficient electron-hole separation. Phenol decomposition occurred mainly *via* superoxide radicals ($^{\bullet}O_2^-$), while the participation of other species, electrons (e^-), holes (h^+), or hydroxyl radicals (•OH) was negligible. The action spectra revealed that the excitation of BiOBr/Bi_2WO_6_1 in the range from 380 to 460 nm caused the photodegradation of phenol, while pristine BiOBr and Bi_2WO_6 exhibited negligible photocatalytic activity excited with a wavelength of 420 nm. After inducing with the wavelength of 420 nm, the AQE of the BiOBr/Bi_2WO_6_1 sample (4.29%) was 8 and 71.5 times higher than those of the pristine BiOBr and Bi_2WO_6 photocatalysts (0.57 and 0.06%, respectively). Thus, the BiOBr/Bi_2WO_6 thin films could be a promising material in photocatalysis application in that those composites could be recycled and reused compared with powder photocatalysts. This research provides a new insight into the design and fabrication of an advanced, highly stable material prepared in IL-assisted systems with enhanced photocatalytic and photoelectrochemical properties under visible irradiation.

CRediT authorship contribution statement

Anna Pancielejko: Investigation, Methodology, Formal analysis, Validation, Data curation, Writing – original draft, Writing – review & editing, Visualization, Funding acquisition. **Justyna Łuczak:** Investigation, Supervision, Visualization, Writing - original draft, Writing - review & editing. **Wojciech Lisowski:** Formal analysis, Investigation, Writing – original draft, Visualization. **Adriana Zaleska-Medynska:** Supervision, Writing - review & editing. **Paweł Mazierski:** Formal analysis, Investigation, Conceptualization, Supervision, Writing – original draft, Visualization.

Declaration of Competing Interest

The authors declare that they have no known competing financial interests or personal relationships that could have appeared to influence the work reported in this paper.

Acknowledgement

This work realises a project co-financed from European Funds 'Integrated Programme of Development of Gdańsk University of Technology', POWR.03.05.00-00-Z044/17.

Appendix A. Supplementary material

Supplementary data to this article can be found online at https://doi.org/10.1016/j.apsusc.2021.151082.

References

[1] X. Meng, Z. Zhang, Bismuth-based photocatalytic semiconductors: Introduction, challenges and possible approaches, J. Mol. Catal. A Chem. 423 (2016) 533–549, https://doi.org/10.1016/j.molcata.2016.07.030.
[2] F. Akira, H. Kenichi, Electrochemical Photolysis of Water at a Semiconductor Electrode, Nature. 238 (1972) 37–38, https://doi.org/10.1038/238037a0.
[3] R.P. Panmand, Y.A. Sethi, S.R. Kadam, M.S. Tamboli, L.K. Nikam, J.D. Ambekar, C.-J. Park, B.B. Kale, Self-assembled hierarchical nanostructures of Bi2WO6 for hydrogen production and dye degradation under solar light, CrystEngComm. 17 (2015) 107–115, https://doi.org/10.1039/c4ce01968g.
[4] C. Zhang, Y. Zhu, Synthesis of square Bi2WO6 nanoplates as high-activity visible-light-driven photocatalysts, Chem. Mater. 17 (2005) 3537–3545, https://doi.org/10.1021/cm0501517.
[5] C. Xu, X. Wei, Z. Ren, Y. Wang, G. Xu, G. Shen, G. Han, Solvothermal preparation of Bi2WO6 nanocrystals with improved visible light photocatalytic activity, Mater. Lett. 63 (2009) 2194–2197, https://doi.org/10.1016/j.matlet.2009.07.014.
[6] G. Zhang, F. Lü, M. Li, J. Yang, X. Zhang, B. Huang, Synthesis of nanometer Bi2WO6 synthesized by sol-gel method and its visible-light photocatalytic activity for degradation of 4BS, J. Phys. Chem. Solids. 71 (2010) 579–582, https://doi.org/10.1016/j.jpcs.2009.12.041.
[7] L. Wu, J. Bi, Z. Li, X. Wang, X. Fu, Rapid preparation of Bi2WO6 photocatalyst with nanosheet morphology via microwave-assisted solvothermal synthesis, Catal. Today. 131 (2008) 15–20, https://doi.org/10.1016/j.cattod.2007.10.089.
[8] S.O. Alfaro, A. Martínez-De La Cruz, Synthesis, characterization and visible-light photocatalytic properties of Bi2WO6 and Bi2W2O9 obtained by co-precipitation method, Appl. Catal. A Gen. 383 (2010) 128–133, https://doi.org/10.1016/j.apcata.2010.05.034.
[9] C. Ng, A. Iwase, Y.H. Ng, R. Amal, Transforming anodized WO3 films into visible-light-active Bi2WO6 photoelectrodes by hydrothermal treatment, J. Phys. Chem. Lett. 3 (2012) 913–918, https://doi.org/10.1021/jz300179k.
[10] X. Zhao, T. Xu, W. Yao, C. Zhang, Y. Zhu, Photoelectrocatalytic degradation of 4-chlorophenol at Bi2WO6 nanoflake film electrode under visible light irradiation, Appl. Catal. B Environ. 72 (2007) 92–97, https://doi.org/10.1016/j.apcatb.2006.10.006.
[11] J. Li, X. Zhang, Z. Ai, F. Jia, L. Zhang, J. Lin, Efficient visible light degradation of Rhodamine B by a photo-electrochemical process based on a Bi2WO6 nanoplate film electrode, J. Phys. Chem. C. 111 (2007) 6832–6836, https://doi.org/doi:10.1021/jp070694z.
[12] Q. Zhang, L. Ma, M. Shao, J. Huang, M. Ding, X. Deng, X. Wei, X. Xu, Anodic oxidation synthesis of one-dimensional TiO2 nanostructures for photocatalytic and field emission properties, J. Nanomater. 2014 (2014), https://doi.org/10.1155/2014/831752.
[13] P. Roy, S. Berger, P. Schmuki, TiO2 nanotubes: Synthesis and applications, Angew. Chemie - Int. Ed. 50 (2011) 2904–2939, https://doi.org/10.1002/anie.201001374.
[14] R. Marschall, Semiconductor composites: Strategies for enhancing charge carrier separation to improve photocatalytic activity, Adv. Funct. Mater. 24 (2014) 2421–2440, https://doi.org/10.1002/adfm.201303214.
[15] D. Kong, X. Ruan, J. Geng, Y. Zhao, D. Zhang, X. Pu, S. Yao, C. Su, 0D/3D ZnIn2S4/Ag6Si2O7 nanocomposite with direct Z-scheme heterojunction for efficient photocatalytic H2 evolution under visible light, Int. J. Hydrogen Energy. 46 (2021) 28043–28052, https://doi.org/10.1016/j.ijhydene.2021.06.053.
[16] Q. Mou, Z. Guo, Y. Chai, B. Liu, C. Liu, Visible-light assisted production of hydrocarbon fuels from carbon dioxide using Cu2O@MnCo2O4 heterojunction, Colloids Surfaces A Physicochem. Eng. Asp. 623 (2021), 126707, https://doi.org/10.1016/j.colsurfa.2021.126707.
[17] J. Low, J. Yu, M. Jaroniec, S. Wageh, A.A. Al-Ghamdi, Heterojunction Photocatalysts, Adv. Mater. 29 (2017), https://doi.org/10.1002/adma.201601694.
[18] M.S. Gui, W. De Zhang, Q.X. Su, C.H. Chen, Preparation and visible light photocatalytic activity of Bi2O3/Bi2WO6 heterojunction photocatalysts, J. Solid State Chem. 184 (2011) 1977–1982, https://doi.org/10.1016/j.jssc.2011.05.057.
[19] P. Ju, P. Wang, B. Li, H. Fan, S. Ai, D. Zhang, Y. Wang, A novel calcined Bi2WO6/BiVO4 heterojunction photocatalyst with highly enhanced photocatalytic activity, Chem. Eng. J. 236 (2014) 430–437, https://doi.org/10.1016/j.cej.2013.10.001.
[20] F. Wang, Y. Gu, Z. Yang, Y. Xie, J. Zhang, X. Shang, H. Zhao, Z. Zhang, X. Wang, The effect of halogen on BiOX (X = Cl, Br, I)/Bi2WO6 heterojunction for visible-light-driven photocatalytic benzyl alcohol selective oxidation, Appl. Catal. A Gen. 567 (2018) 65–72, https://doi.org/10.1016/j.apcata.2018.09.010.
[21] P. Kar, T.K. Maji, R. Nandil, P. Lemmens, S.K. Pal, In-situ hydrothermal synthesis of Bi-Bi2O2CO3 heterojunction photocatalyst with enhanced visible light photocatalytic activity, Nano-Micro Lett. 9 (2017) 1–10, https://doi.org/10.1007/s40820-016-0118-0.
[22] J. Guo, X. Liao, M.H. Lee, G. Hyett, C.C. Huang, D.W. Hewak, S. Mailis, W. Zhou, Z. Jiang, Experimental and DFT insights of the Zn-doping effects on the visible-light photocatalytic water splitting and dye decomposition over Zn-doped BiOBr photocatalysts, Appl. Catal. B Environ. 243 (2019) 502–512, https://doi.org/10.1016/j.apcatb.2018.09.089.
[23] Q. Nan, S. Huang, Y. Zhou, S. Zhao, M. He, Y. Wang, S. Li, T. Huang, W. Pan, Ionic liquid-assisted synthesis of porous BiOBr microspheres with enhanced visible light photocatalytic performance, Appl. Organomet. Chem. 32 (2018) 1–13, https://doi.org/10.1002/aoc.4596.
[24] J. Łuczak, M. Paszkiewicz, A. Krukowska, A. Malankowska, A. Zaleska-Medynska, Ionic liquids for nano- and microstructures preparation. Part 1: Properties and multifunctional role, Adv. Colloid Interface Sci. 230 (2016) 13–28, https://doi.org/10.1016/j.cis.2015.08.006.
[25] J. Łuczak, M. Paszkiewicz-Gawron, M. Długokęcka, W. Lisowski, E. Grabowska, S. Makurat, J. Rak, A. Zaleska-Medynska, Visible-light photocatalytic activity of ionic liquid TiO2 spheres: Effect of the ionic liquid's anion structure, ChemCatChem. 9 (2017) 4377–4388, https://doi.org/10.1002/cctc.201700861.
[26] M. Paszkiewicz, J. Łuczak, W. Lisowski, P. Patyk, A. Zaleska-Medynska, The ILs-assisted solvothermal synthesis of TiO2 spheres: The effect of ionic liquids on morphology and photoactivity of TiO2, Appl. Catal. B Environ. 184 (2016) 223–237, https://doi.org/10.1016/J.APCATB.2015.11.019.
[27] J. Yu, Q. Li, S. Liu, M. Jaroniec, Ionic-liquid-assisted synthesis of uniform fluorinated B/C-codoped TiO2 nanocrystals and their enhanced visible-light photocatalytic activity, Chem. - A Eur. J. 19 (2013) 2433–2441, https://doi.org/10.1002/chem.201202778.
[28] M. Paszkiewicz-Gawron, M. Długokęcka, W. Lisowski, M.C. Paganini, E. Giamello, T. Klimczuk, M. Paszkiewicz, E. Grabowska, A. Zaleska-Medynska, J. Luczak, Dependence between ionic liquid structure and mechanism of visible-light-induced activity of TiO 2 obtained by ionic-liquid-assisted solvothermal synthesis, ACS Sustain. Chem. Eng. 6 (2018) 3927–3937, https://doi.org/10.1021/acssuschemeng.7b04291.
[29] J. Xia, J. Zhang, S. Yin, H. Li, H. Xu, L. Xu, Q. Zhang, Advanced visible light photocatalytic properties of BiOCl micro/nanospheres synthesized via reactable ionic liquids, J. Phys. Chem. Solids. 74 (2013) 298–304, https://doi.org/10.1016/j.jpcs.2012.10.002.
[30] Q. Jiang, M. Ji, R. Chen, Y. Zhang, K. Li, C. Meng, Z. Chen, H. Li, J. Xia, Ionic liquid induced mechanochemical synthesis of BiOBr ultrathin nanosheets at ambient temperature with superior visible-light-driven photocatalysis, J. Colloid Interface Sci. 574 (2020) 131–139, https://doi.org/10.1016/j.jcis.2020.04.018.
[31] A. Bielicka-Giełdoń, P. Wilczewska, A. Malankowska, K. Szczodrowski, J. Ryl, A. Zielińska-Jurek, E.M. Siedlecka, Morphology, surface properties and photocatalytic activity of the bismuth oxyhalides semiconductors prepared by ionic liquid assisted solvothermal method, Sep. Purif. Technol. 217 (2019) 164–173, https://doi.org/10.1016/j.seppur.2019.02.031.
[32] X. Meng, Z. Zhang, Facile synthesis of BiOBr/Bi2WO6 heterojunction semiconductors with high visible-light-driven photocatalytic activity, J. Photochem. Photobiol. A Chem. 310 (2015) 33–44, https://doi.org/10.1016/j.jphotochem.2015.04.024.
[33] X. Meng, Z. Zhang, Synthesis, analysis, and testing of BiOBr-Bi2WO6 photocatalytic heterojunction semiconductors, Int. J. Photoenergy. 2015 (2015), https://doi.org/10.1155/2015/630476.
[34] P. Dumrongrojthanath, A. Phuruangrat, K. Doungarno, T. Thongtem, P. Patiphatpanya, S. Thongtem, Microwave-hydrothermal synthesis of BiOBr/Bi2WO6 nanocomposites for enhanced photocatalytic performance, Ceram. Int. 44 (2018) S148–S151, https://doi.org/10.1016/j.ceramint.2018.08.128.
[35] J. Xia, J. Di, S. Yin, H. Xu, J. Zhang, Y. Xu, L. Xu, H. Li, M. Ji, Facile fabrication of the visible-light-driven Bi2WO6/BiOBr composite with enhanced photocatalytic activity, RSC Adv. 4 (2014) 82–90, https://doi.org/10.1039/c3ra44191a.
[36] X. Ren, K. Wu, Z. Qin, X. Zhao, H. Yang, The construction of type II heterojunction of Bi2WO6/BiOBr photocatalyst with improved photocatalytic performance, J. Alloys Compd. 788 (2019) 102–109, https://doi.org/10.1016/j.jallcom.2019.02.211.
[37] J. He, Y. Liu, M. Wang, Y. Wang, F. Long, Ionic liquid-hydrothermal synthesis of Z-scheme BiOBr/Bi2WO6 heterojunction with enhanced photocatalytic activity, J. Alloys Compd. 865 (2021), 158760, https://doi.org/10.1016/j.jallcom.2021.158760.
[38] A. Pancielejko, M. Rzepnikowska, A. Zaleska-Medynska, J. Łuczak, P. Mazierski, Enhanced Visible Light Active WO3 Thin Films Toward Air Purification: Effect of the Synthesis Conditions, Materials (Basel). 13 (2020) 1–18, https://doi.org/10.3390/ma13163506.
[39] O. Henry, Natacha; Evain, Michel; Deniard. Philippe; Jobic, Stephane, Abraham, Francis; Mentre, [Bi2O2]2+ Layers in Bi2O2(OH)(NO3): Synthesis and Structure Determination, Verlag Der Zeitschrift Für Naturforsch. 2 (2014) 322–327. https://doi.org/10.1515/znb-2005-0315.
[40] A. V. Naumkin, A. Kraut-Vass, S.W. Gaarenstroom, C.J. Powell, NIST X-ray Photoelectron Spectroscopy Database 20 Version 4.1.2012, (2012).
[41] Y. Lv, W. Yao, R. Zong, Y. Zhu, Fabrication of wide-range-visible photocatalyst Bi2WO6-x nanoplates via surface oxygen vacancies, Sci. York. 6 (2016) 1–9, https://doi.org/10.1038/srep19347.
[42] L.H. Hoang, N.D. Phu, H. Peng, X.B. Chen, High photocatalytic activity N-doped Bi2WO6 nanoparticles using a two-step microwave-assisted and hydrothermal synthesis, J. Alloys Compd. 744 (2018) 228–233, https://doi.org/10.1016/j.jallcom.2018.02.094.

[43] G. Jiang, X. Li, Z. Wei, T. Jiang, X. Du, W. Chen, Growth of N-doped BiOBr nanosheets on carbon fi bers for photocatalytic degradation of organic pollutants under visible light irradiation, Powder Technol. 260 (2014) 84–89, https://doi.org/10.1016/j.powtec.2014.04.005.
[44] X. Zhang, C.Y. Wang, L.W. Wang, G.X. Huang, W.K. Wang, H.Q. Yu, Fabrication of BiOBrxI1-x photocatalysts with tunable visible light catalytic activity by modulating band structures, Sci. Rep. 6 (2016) 2–11, https://doi.org/10.1038/srep22800.
[45] H.W. Tien, Y.L. Huang, S.Y. Yang, J.Y. Wang, C.C.M. Ma, The production of graphene nanosheets decorated with silver nanoparticles for use in transparent, conductive films, Carbon N. Y. 49 (2011) 1550–1560, https://doi.org/10.1016/j.carbon.2010.12.022.
[46] H. Sudrajat, Template-free, simple fabrication of C/N-doped Bi2O3 nanospheres with appreciable photocatalytic activity under visible light, Superlattices Microstruct. 109 (2017) 229–239, https://doi.org/10.1016/j.spmi.2017.05.010.
[47] G. Jiang, X. Li, Z. Wei, T. Jiang, X. Du, W. Chen, Growth of N-doped BiOBr nanosheets on carbon fibers for photocatalytic degradation of organic pollutants under visible light irradiation, Powder Technol. 260 (2014) 84–89, https://doi.org/10.1016/j.powtec.2014.04.005.
[48] J.S. Stevens, A.C. De Luca, M. Pelendritis, G. Terenghi, S. Downes, S.L. M. Schroeder, Quantitative analysis of complex amino acids and RGD peptides by X-ray photoelectron spectroscopy (XPS), Surf. Interface Anal. 45 (2013) 1238–1246, https://doi.org/10.1002/sia.5261.
[49] J. Fu, Y. Tian, B. Chang, F. Xi, X. Dong, BiOBr-carbon nitride heterojunctions: Synthesis, enhanced activity and photocatalytic mechanism, J. Mater. Chem. 22 (2012) 21159–21166, https://doi.org/10.1039/c2jm34778d.
[50] G.H. He, G.L. He, A.J. Li, X. Li, X.J. Wang, Y.P. Fang, Y.H. Xu, Synthesis and visible light photocatalytic behavior of WO3 (core)/Bi2WO6 (shell), J. Mol. Catal. A Chem. 385 (2014) 106–111, https://doi.org/10.1016/j.molcata.2014.01.022.
[51] M. Ge, L. Liu, Sunlight-induced photocatalytic performance of Bi2WO6 hierarchical microspheres synthesized via a relatively green hydrothermal route, Mater. Sci. Semicond. Process. 25 (2014) 258–263, https://doi.org/10.1016/j.mssp.2013.12.026.
[52] R. Adhikari, H.M. Trital, A. Rajbhandari, J. Won, S.W. Lee, Microwave induced morphology evolution of bismuth tungstate photocatalyst: Evaulation of phocatalytic activity under visible light, J. Nanosci. Nanotechnol. 15 (2015) 7249–7253, https://doi.org/10.1166/jnn.2015.10576.
[53] Z. Zhu, Y. Yan, J. Li, Preparation of flower-like BiOBr-WO3-Bi2WO6 ternary hybrid with enhanced visible-light photocatalytic activity, Elsevier Ltd (2015), https://doi.org/10.1016/j.jallcom.2015.08.137.
[54] J. Hu, W. An, H. Wang, J. Geng, W. Cui, Y. Zhan, Synthesis of a hierarchical BiOBr nanodots/Bi2WO6 p–n heterostructure with enhanced photoinduced electric and photocatalytic degradation performance, RSC Adv. 6 (2016) 29554–29562, https://doi.org/10.1039/c6ra00794e.
[55] D. Liu, J.C. Liu, W. Cai, J. Ma, H. Bin Yang, H. Xiao, J. Li, Y. Xiong, Y. Huang, B. Liu, Selective photoelectrochemical oxidation of glycerol to high value-added dihydroxyacetone, Nat. Commun. 10 (2019), https://doi.org/10.1038/s41467-019-09788-5.
[56] X. Xu, X. Yu, L. Mao, S.P. Yang, Z. Peng, Preparation and photoluminescence of Bi3+-doped strontium chloroapatite nano-phosphor, Mater. Lett. 58 (2004) 3665–3668, https://doi.org/10.1016/j.matlet.2004.04.037.
[57] S. Zhu, C. Yang, F. Li, T. Li, M. Zhang, W. Cao, Improved photocatalytic Bi2WO6/BiOCl heterojunctions: One-step synthesis via an ionic-liquid assisted ultrasonic method and first-principles calculations, Mol. Catal. 435 (2017) 33–48, https://doi.org/10.1016/j.mcat.2017.03.016.
[58] W. Yang, B. Ma, W. Wang, Y. Wen, D. Zeng, B. Shan, Enhanced photosensitized activity of a BiOCl-Bi2WO6 heterojunction by effective interfacial charge transfer, Phys. Chem. Chem. Phys. 15 (2013) 19387–19394, https://doi.org/10.1039/c3cp53628a.
[59] H. Li, Y. Cui, W. Hong, High photocatalytic performance of BiOI/Bi2WO6 toward toluene and Reactive Brilliant Red, Appl. Surf. Sci. 264 (2013) 581–588, https://doi.org/10.1016/j.apsusc.2012.10.068.
[60] Y. Ma, Z. Chen, D. Qu, J. Shi, Synthesis of chemically bonded BiOCl@Bi2WO6 microspheres with exposed (020) Bi2WO6 facets and their enhanced photocatalytic activities under visible light irradiation, Appl. Surf. Sci. 361 (2016) 63–71, https://doi.org/10.1016/j.apsusc.2015.11.130.
[61] D. Kong, H. Fan, D. Yin, D. Zhang, X. Pu, S. Yao, C. Su, AgFeO2 nanoparticle/ZnIn2S4 microsphere p-n heterojunctions with hierarchical nanostructures for efficient visible-light-driven H2 evolution, ACS Sustain. Chem. Eng. 9 (2021) 2673–2683, https://doi.org/10.1021/acssuschemeng.0c07638.